

## Tunable exciton–polariton condensation in a two-dimensional Lieb lattice at room temperature

Fabio Scafirimuto<sup>1</sup>, Darius Urbonas <sup>1</sup>, Michael A. Becker <sup>1,3</sup>, Ullrich Scherf <sup>2</sup>, Rainer F. Mahrt <sup>1</sup> & Thilo Stöferle <sup>1</sup>✉

Microcavities with embedded optically active materials allow to create exciton–polariton condensates in the strong light–matter interaction regime. These condensates exhibit quantum fluid properties up to room temperature, and, when crystal-like lattices are imprinted in the cavity, they can be used to emulate and study solid-state physics toy models. Here, we demonstrate room temperature polariton condensation in a nano-fabricated two-dimensional Lieb lattice with an organic polymer. We exploit the tunability of our open cavity to selectively condense into the *s*-, *p*- and *d*-lattice band manifolds. Furthermore, we interferometrically measure long-range first-order coherence across the lattice and assess the influence of the disorder in the system. These are key first steps to investigate extended topological polariton systems at ambient conditions.

<sup>1</sup>IBM Research Europe – Zurich, Säumerstrasse 4, Rüschlikon, Switzerland. <sup>2</sup>Macromolecular Chemistry Group and Institute for Polymer Technology, Bergische Universität Wuppertal, Gauss-Strasse 20, Wuppertal, Germany. <sup>3</sup>Present address: Max Planck Institute for the Science of Light, Staudtstrasse 2, Erlangen, Germany. ✉email: [tof@zurich.ibm.com](mailto:tof@zurich.ibm.com)

The interest in experimentally well-controllable, artificial model systems has grown over the past decade in order to explore fundamental properties of exotic states of matter<sup>1</sup> as well as testing the boundaries of present models for solid state physics and material science through quantum simulations<sup>2</sup>. Motivated by the remarkable achievements with ultracold atomic gases<sup>3</sup>, simulators based on solid-state systems using photonic structures have received increasing attention recently<sup>4</sup>. When an optically active material is placed between highly reflective mirrors of a microcavity and the photon loss and exciton decay rates are smaller than the light-matter coupling rate, new eigenstates supporting exciton-polariton quasi-particles arise. At sufficiently high density and low temperature, polariton condensates can be formed, which are macroscopically coherent quantum fluids<sup>5</sup>. Whereas many common inorganic semiconductor polariton devices are limited to cryogenic operation, these condensates can be created even at room temperature when using organic materials<sup>6,7</sup> while retaining their superfluid properties<sup>8</sup>.

By subjecting polaritons to periodic lattice potentials, as has recently been achieved even at room temperature<sup>9,10</sup>, a large variety of Hamiltonians can be studied<sup>11,12</sup>. As model systems for two-dimensional (2D) and topological materials, lattice geometries with band structures that feature Dirac cones<sup>13</sup>, flat bands, and topological edge states<sup>14</sup> are of interest<sup>15</sup>. Particularly Lieb lattices have been extensively studied due to their rich ferromagnetic<sup>16</sup> and topological properties that enable them to host exotic phenomena like quantum anomalous Hall effect<sup>17</sup> and enhanced superfluidity<sup>18</sup>. Exploiting effective spin-orbit coupling through polarization-dependent coupling<sup>19,20</sup>, polariton condensation into the *s*- and *p*-bands of 2D Lieb lattices has been observed with inorganic semiconductor cavities at cryogenic temperature<sup>21,22</sup>.

Lattice potentials and other potential landscapes for polaritons have been created by locally modifying the photonic cavity resonance wavelength using various techniques like lithographic definition<sup>23</sup> or laser excitation<sup>24</sup>. More recently, tunable open cavities in which the two cavity halves are mounted on separate nanopositioning stages have allowed to readily change the cavity resonance wavelength, as has already been demonstrated in experiments where polaritons were confined within single<sup>20</sup> and double nanostructured potential wells<sup>25</sup>. Furthermore, compared to static cavity arrays<sup>26,27</sup>, tunable open cavities enable to use the very same photonic lattice structure at several locations of the active material layer by simply moving only one half of the cavity with respect to the other. This allows to assess the disorder and to determine if it originates from the photonic structure or the active material.

Here, we use cavities filled with emissive polymer beyond the single zero-dimensional polariton condensate regime<sup>28</sup> and realize extended lattices with polariton condensates at room temperature. By tuning the cavity length, we are able to selectively form condensates in the *s*-, *p*- or *d*-band manifolds of the 2D Lieb lattice. We measure first order coherence and observe condensate fragmentation due to disorder in the polymer. Our experiments showcase a versatile polariton simulator platform that allows to study interesting, complex Hamiltonians at ambient conditions.

## Results

We pattern a dense array of Gaussian deformations into one of the mirror substrates (Fig. 1a and Methods) that effectively forms a 2D Lieb lattice with a square-depleted unit cell composed of A, B and C sites (Fig. 1b). On top, a distributed Bragg reflector (DBR) is deposited. The other cavity half is fabricated by depositing the DBR and a thin spacer layer on a flat substrate followed by spin-coating a conjugated ladder-type polymer called

MeLPPP (see Methods and Supplementary Figs. 1–3). The stack is completed with a protective layer against photooxidation and sticking, but whose deposition induces some defects in the MeLPPP layer (see Supplementary Fig. 2). Both cavity halves are then mounted on separate XYZ positioning stages. In very similar cavities with just a single Gaussian deformation we determined the light-matter coupling strength to be on the order of  $2\Omega = 100\text{--}150\text{ meV}$  by tuning the photonic cavity mode with respect to the exciton and fitting the Rabi splitting<sup>25,28</sup>. For the lattice structure, we assume a similar coupling strength, however, a direct measurement is not feasible due to the intricate band structure of the lattice.

**Polaritons in the 2D Lieb lattice.** First, we use a weak off-resonant continuous-wave excitation and observe the polariton emission by imaging the sample in Fourier space onto the entrance slit of a monochromator that is aligned along the A–B axis of the lattice. This reveals the Lieb lattice dispersion relation of the *s*-, *p*- and *d*-band manifolds along the  $\Gamma$ –X direction (Fig. 1c). Notably, the far field emission does not show the entire band structure from the tight-binding model (see Supplementary Note 1 for more details) as some sections and bands are missing or dim due to the polariton population not filling homogeneously all states<sup>22</sup>. Furthermore, broadening makes it difficult to resolve individual bands within the *s*-manifold, whereas in the energetically wider *p*-manifold the shape of the individual bands can be inferred better. There are several reasons for this broadening: The finite polariton lifetime smears out the bands and leads to a highly inhomogeneous intensity distribution<sup>22</sup>. Moreover, the fabricated lattice comprises only 5.5 unit cells in both directions, and hence, broadening and reduced band gaps can be expected due to finite-size effects. From the fact that we can observe narrow condensate line widths (see further below), we can exclude that mechanical vibrations are responsible for the broadening of the bands. Compared to polariton lattices with inorganic semiconductors in microcavities with a quality factor *Q* of several tens of thousands<sup>22,26</sup>, our *Q* ~ 600 leads to a lifetime of the order of 200 fs, effectively resulting in the overlapping and blending of flat and dispersive bands.

To unambiguously identify the characteristic modes<sup>21,22</sup>, we investigate the spatial distribution of polaritons in the lattice. We observe the real space images corresponding to the individual bands by exploiting the capability to tune the cavity length. Herewith we can alter the maximum of the emission within the band structure while additionally suppressing the other bands using a <5 meV-narrow, tunable spectral filter. The resulting real-space images of the polariton emission are shown in Fig. 2a–c, where the characteristic mode patterns of *s*-, *p*- and *d*-bands are clearly visible. A movie that shows the evolution of mode patterns during the tuning of the cavity resonance can be found as Supplementary Movie 1. By observing the real-space images of the individual bands it is evident that a spatial inhomogeneity of the emission pattern exists, apart from the inhomogeneity that is superimposed by the beam profile of the excitation beam. We attribute this inhomogeneity to disorder in the system<sup>26,29,30</sup>, which can also affect the establishment of long-range Bloch modes.

**Tunable polariton condensation.** Next, we drive the system in the condensate regime by changing the excitation to a pulsed amplified laser source with 400-nm excitation wavelength (see Methods). Above the condensation threshold, the emission intensity increases nonlinearly, as will be studied in more detail further below. The filtered real-space images of condensates in the *s*-, *p*- and *d*-band manifolds are shown in Fig. 2d–f, respectively.

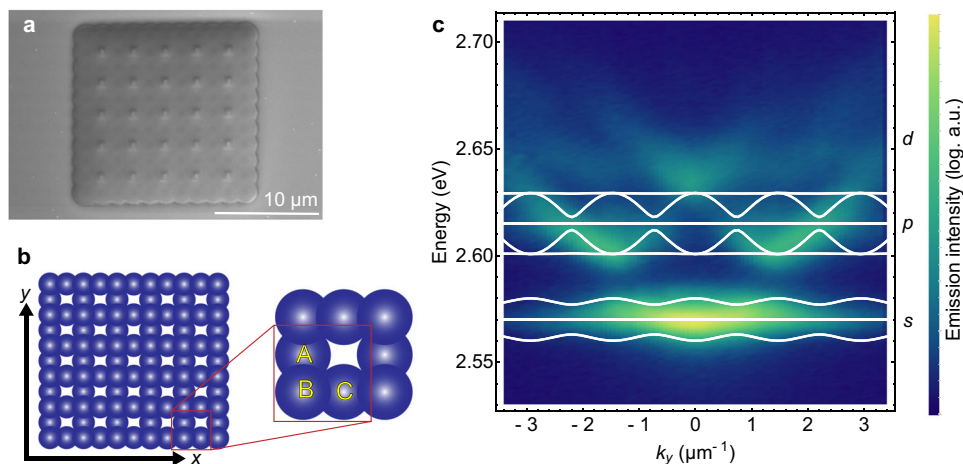


**Fig. 1 Two-dimensional Lieb lattice.** **a** Scanning electron microscopy image of the fabricated lattice structure. **b** Schematic illustration of the two-dimensional Lieb lattice consisting of  $5.5 \times 5.5$  unit cells, each comprising three different sites (labelled A, B, C in the zoom-in). **c** Polariton emission as a function of energy obtained with weak off-resonant excitation and Fourier-space imaging onto the entrance slit of a monochromator. This effectively shows the polariton population in the lattice's dispersion relation versus the  $k_y$  wavevector component in the  $\Gamma - X$  direction. The superimposed white lines show the calculated  $s$ - and  $p$ -band manifolds, as detailed in Supplementary Note 1.

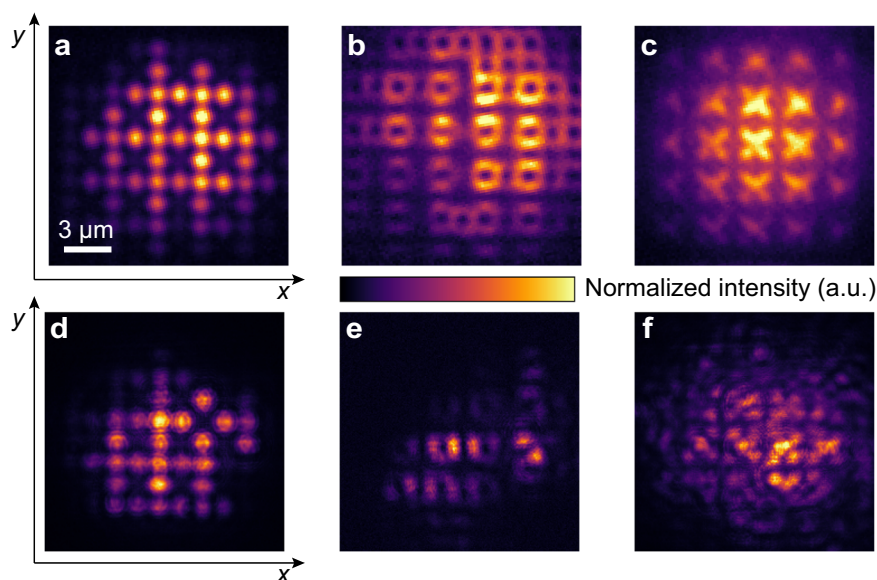


**Fig. 2 Populating different bands and selective condensation by tuning the microcavity.** **a-c** Real-space images ( $15 \times 15 \mu\text{m}$ ) of the polariton emission show dominant population of the  $s$ -band (**a**),  $p$ -band (**b**) and  $d$ -band (**c**) as the cavity length is tuned longer. The images are obtained with weak off-resonant excitation and by filtering out the other bands by using a tunable bandpass spectral filter. **d-f** Real-space images of the emission in the  $s$ - (**d**),  $p$ - (**e**) and  $d$ -bands (**f**), respectively, at an excitation density above the condensation threshold. Note that the position on the polymer layer can vary between the different measurements.

The three characteristic modes are clearly visible, and the patterns match the ones observed below threshold. However, the inhomogeneity of the emission patterns becomes more pronounced, indicating that the polariton condensate regime is more sensitive to disorder. Our open cavity configuration, where we can independently move the cavity half with the active polymer layer relatively to the other cavity half with the photonic lattice structure, allows to probe whether the disorder of the lattice or of the polymer dominates. We conclude that the dominating disorder comes from the polymer because for the same photonic lattice structure, the intensity distributions change significantly when we realize condensates at different positions on the polymer layer.

To investigate the first-order spatial coherence we perform measurements with a Michelson interferometer by interfering the real-space image of the condensate with the centrosymmetric copy of itself. In Fig. 3 we report two interferograms observed for the  $s$ - and the  $p$ -bands. In Fig. 3a, the spatial coherence of the  $s$ -band spreads over 6 lattice sites in one direction and 3 lattice sites in the other. The first-order coherence measurement for the  $p$ -band reported in Fig. 3b shows similar results. By repeating this type of measurements for several polymer positions without changing the lattice or excitation conditions, we observe first-order spatial coherence extension varying from 1-2 up to 7 lattice sites. Thus, this varying spatial extension of the first-order coherence supports the hypothesis that the inhomogeneity of the

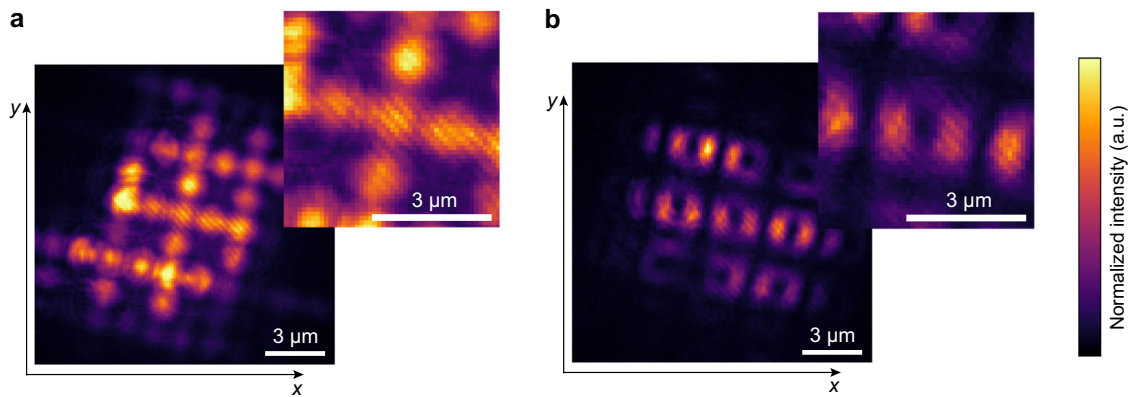


**Fig. 3 First-order coherence of the condensate in the Lieb lattice.** **a** Real-space interferogram ( $15 \times 15 \mu\text{m}$ ) of an exciton-polariton condensate in the  $s$ -band using a Michelson interferometer equipped with a retroreflector in one arm. The spatially inverted copy is interfered with the original image from the other arm with the B lattice site in its center. The inset shows a  $2\times$  zoom into the central site and the fringe pattern. The spatial first-order coherence extends over several lattice sites but exhibits spatially inhomogeneous distributions due to the polymer disorder that vary also between different polymer positions. **b** Similar interferogram obtained when tuning the cavity to result in condensation in the  $p$ -band.

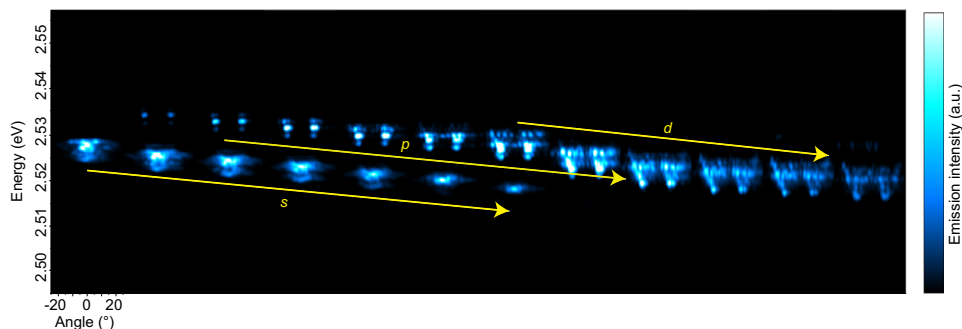


**Fig. 4 Condensation in the lattice's dispersion relation while tuning the microcavity.** Sequence of Fourier-space images obtained at a constant excitation density above condensation threshold. The length of the cavity is increased from left to right, bringing first the  $s$ -band in resonance with the vibronic relaxation that is most effective near 2.53 eV (200 meV below the exciton reservoir), then the  $p$ -band (near the middle) and finally the  $d$ -band. The smearing and fragmentation of the bands is caused by fragmentation of the condensates due to disorder.

polymer on the micrometer scale eventually leads to fragmentation of the condensates.

For examining further why the spatial extension of the first-order coherence (Fig. 3) appears to be considerably smaller than the real-space images in the condensate regime suggest (Fig. 2d–f), we study the angle- and energy-resolved emission, i.e., the polariton population within the dispersion relation, similar to Fig. 1c but now above condensation threshold. In Fig. 4 we report the results of this experiment by showing a series of dispersion relation images taken sequentially at constant excitation fluence while moving the two cavity halves apart, effectively tuning the cavity resonance by about 20 meV. As the condensates only form at certain points of the dispersion relation, the clear assignment to specific bands is only possible due to comparison with real-space images obtained at similar respective cavity length, allowing to observe the distinct mode symmetry. At first, the emission stems only from condensation in the  $s$ -band, then for increasingly larger separation of the cavity halves the  $p$ -band becomes dominant, while the  $s$ -band fades. At even larger cavity lengths the  $d$ -band appears, then dominates and eventually also fades away.

**Condensate modes and fragmentation.** This data shows that the fragmentation of condensates is much more apparent in the dispersion relation than in real-space images. The scatter in the condensate energy explains why the interference experiments show only limited and varying long-range phase coherence.

Compared to the dispersion relation below threshold where the bands appeared just broadened, the condensate regime with its narrow emission lines is a much more sensitive probe for the disorder. Since this fragmentation changes with the polymer position, also this effect seems to be dominated by intrinsic material disorder. So, either locally the effective local cavity resonance energy is modified (by variations in layer thickness, density or defects) or the exciton energies vary (through aggregates or traps). The disorder in such extended array of over  $10 \times 10 \mu\text{m}$  spreads the emitted photon energies over several meV, whereas the condensate emission linewidth in a single, 1- $\mu\text{m}$  wide Gaussian defect<sup>28</sup> can get as low as 300  $\mu\text{eV}$ .

For investigating the condensation threshold and the nonlinear behaviour of different bands we acquire a set of angle-resolved high-resolution spectra (see Methods) while gradually increasing the excitation fluence at fixed cavity detuning. By integrating each image over the angular dimension, we obtain the spectral emission characteristics plotted versus the excitation fluence in Fig. 5. For this measurement, we tune the cavity such that both  $s$ - and  $p$ -band condensates can be observed simultaneously. It is evident that there is a competition between several  $s$ -like and  $p$ -like modes and that both appear fragmented due to disorder. The fact that modes belonging to the  $s$ -band manifold have a slightly lower threshold of  $\sim 500 \mu\text{J cm}^{-2}$  than the modes belonging to the  $p$ -band manifold of  $\sim 650 \mu\text{J cm}^{-2}$  is affected by the choice of the cavity detuning. Figure 5b–d represent three examples of the underlying angle-resolved spectra for different values of the

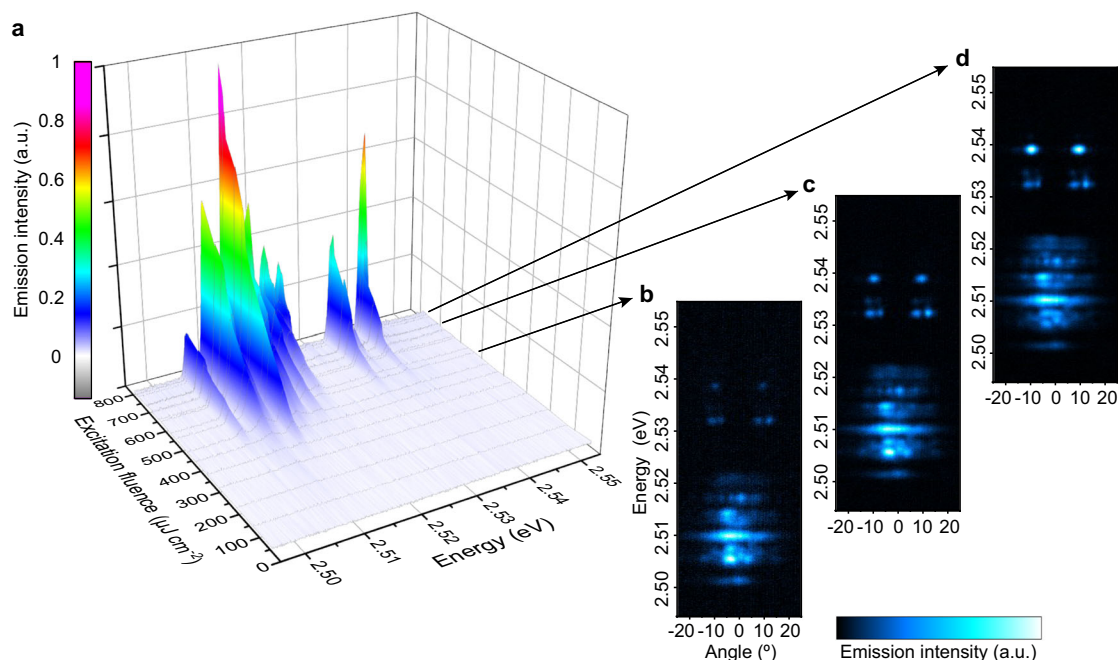


**Fig. 5 Nonlinear intensity increase and fragmentation in energy.** **a** The cavity length is tuned such that both *s*- and *p*-band condensates are observed. The modes between 2.50 and 2.52 eV exhibit *s*-like symmetry, and the modes above 2.53 eV are *p*-like. The angle-integrated emission spectra are shown as a function of excitation fluence. **b–d** Fourier-space images at different fluences. At about  $500 \mu\text{J cm}^{-2}$  all the *s*-like modes start to condense (**b**), then at higher fluence around  $650 \mu\text{J cm}^{-2}$  the condensation into *p*-like modes set in **c** which then increase further (**d**). Obviously, mode competition changes the relative intensity between the condensate modes. At this particular polymer position the disorder is so pronounced that the *s*-condensates are fragmented over more than 10 meV in energy and also over the angle around zero in-plane wavevector.

excitation fluence that resemble the rich multimode behavior as displayed in Fig. 4. It is remarkable that despite the system's disorder the thresholds within the manifold of fragmented condensate modes seem rather similar, independent of position, mode symmetry and emitted photon energy and are mostly dependent only on the overall cavity detuning. The difference in the slopes above threshold and that some of them change at higher fluence suggests an underlying complex competition between several modes during the condensation process. Notably, the amount of blueshift is also similar for all modes (1–2 meV in the excitation fluence range studied), as expected from the underlying saturation mechanism<sup>31</sup> that is the same for all kinds of modes.

## Discussion

The observation that we can selectively condense into different modes exploits a unique feature of organic polariton condensates: The relaxation from the exciton reservoir and thereby the condensation is promoted when the energetic difference between the excitons and the polariton state matches the energy of a vibronic excitation in the material<sup>32–34</sup>. Hence, when the polariton energy is adjusted by changing in situ the length of the cavity, this does not only change the wavefunction composition between a more photonic and a more excitonic nature but leads to much more profound effects from the change in the relaxation, too.

While below threshold the band structure measurements reveal long-range extended Bloch states, even small energetic disorder becomes more pronounced above threshold due to the non-linearity of the condensate. This leads to fragmentation and consequently to a reduction of the observed spatial coherence length. Remarkably, such fragmentation is not observed in similar monolithic cavities with the same MeLPPP polymer but without lattice<sup>6</sup>. Hence, as the principle fabrication steps for the polymer layer are similar and should not lead to substantially changed

amount of disorder in the polymer, it is the condensation process in the complex mode structure of the lattice itself that leads to larger sensitivity to the disorder and consequently to fragmentation. The fragility and susceptibility towards disorder-induced localization of flat band condensates is well-known in the literature<sup>26,29,30</sup>. Nevertheless, despite these experimental challenges, flat band systems remain interesting because of their topological properties<sup>17,35</sup> and other exotic features like gap solitons<sup>30</sup>.

In conclusion, we have demonstrated a versatile experimental platform to study polariton quantum fluids in extended, two-dimensional lattices at room temperature. We have tuned the cavity to force condensation in *s*-, *p*- and *d*-band manifolds, as evidenced by real- and Fourier-space imaging as well as studying the nonlinear intensity increase and the first-order spatial coherence. The experiments with these tunable open-access cavities pave the way for exploring complex lattice Hamiltonians, e.g. supporting topologically protected modes, with polaritons at room temperature and the influence of disorder.

## Methods

**Fabrication.** The tunable microcavity consists of two separate halves. For the lower half, we use a fused silica substrate and deposit a DBR with 9.5 layer pairs of  $\text{Ta}_2\text{O}_5/\text{SiO}_2$  quarter-wave layers with a stop-band center at 475 nm and a 30 nm spacer layer of  $\text{SiO}_2$  using ion beam deposition. Then we spin-coat a 35 nm-thin layer from a solution of 1%wt of methyl-substituted ladder-type poly(*p*-phenylene) (MeLPPP) dissolved in toluene. For preventing photo-degradation and sticking of material when the cavity halves touch, we add 10 nm of  $\text{SiO}_2$  by magnetron sputtering. For the upper half, we start with a borosilicate substrate and etch about 30  $\mu\text{m}$  deep around a mesa of 200  $\mu\text{m}$  diameter using HF. Then we pattern the lattice structure containing 96 Gaussian defects (45 nm deep, 1060 nm full-width at half-maximum (FWHM), 1400 nm center-to-center distance) forming the 2D Lieb lattice by focused ion beam milling. Subsequently, we deposit the DBR with 6.5 layer pairs of  $\text{Ta}_2\text{O}_5/\text{SiO}_2$ .

**Characterization.** The two cavity halves are mounted on separate XYZ nanopositioning stages (the smaller stage for the top half is mounted on the stage for the

bottom half, thereby reducing non-common-mode vibrations) with additional control of their relative tilt angles, located in an environment with passive acoustic isolation (Angst+Pflister APSOvib® body sound damping plate, damping frequencies in the range 100–4000 Hz), and active mechanical vibration cancellation (TableStable TS-300, actively cancelling frequencies below 300 Hz) but otherwise ambient conditions. In the weak excitation regime, we use a 405 nm diode laser coupled to a single-mode fiber. For excitation into the condensate regime we couple a frequency-doubled, amplified laser at 400 nm with ~150 fs pulse duration and 1 kHz repetition rate into a single-mode photonic crystal fiber. We use a quarter-wave plate to scramble the linear polarization and a 10× microscope objective to achieve a Gaussian excitation spot with 15 μm FWHM. We collect the emitted light from the other side through the lower cavity half with a 20× objective. The band structure measurements are done by focusing the Fourier plane image onto the entrance slit of a 0.5 m-long monochromator (equipped with gratings with 300 and 1800 lines per mm) with attached cooled, back-illuminated charged-coupled device (CCD) camera. The orientation of the reciprocal lattice images is aligned with a dove prism to match the slit orientation. Real-space images are recorded by focusing the emitted light onto another cooled CCD camera, in front of which optionally a Michelson interferometer with adjustable path length difference and a retroreflector can be placed. For single-band measurements (real-space and angle-resolved spectra) we use two angle-tunable bandpass filters (passband of 15 nm FWHM) in series to effectively achieve 5 meV spectral passband filter width with steep edges in the detection path.

### Data availability

The raw and analyzed data that support the findings of this study are available from the corresponding author upon reasonable request.

Received: 10 September 2020; Accepted: 28 January 2021;

Published online: 01 March 2021

### References

- Leykam, D., Andreanov, A. & Flach, S. Artificial flat band systems: from lattice models to experiments. *Adv. Phys.* **3**, 1473052 (2018).
- Buluta, I. & Nori, F. Quantum simulators. *Science* **326**, 108–111 (2009).
- Gross, C. & Bloch, I. Quantum simulations with ultracold atoms in optical lattices. *Science* **357**, 995–1001 (2017).
- Quantum Simulations with Photons and Polaritons: Merging Quantum Optics with Condensed Matter Physics*. (Springer International Publishing, 2017).
- Carusotto, I. & Ciuti, C. Quantum fluids of light. *Rev. Mod. Phys.* **85**, 299–366 (2013).
- Plumhof, J. D., Stöferle, T., Mai, L., Scherf, U. & Mahrt, R. F. Room-temperature Bose–Einstein condensation of cavity exciton–polaritons in a polymer. *Nat. Mater.* **13**, 247–252 (2014).
- Daskalakis, K. S., Maier, S. A., Murray, R. & Kéna-Cohen, S. Nonlinear interactions in an organic polariton condensate. *Nat. Mater.* **13**, 271–278 (2014).
- Lerario, G. et al. Room-temperature superfluidity in a polariton condensate. *Nat. Phys.* **13**, 837–841 (2017).
- Su, R. et al. Observation of exciton polariton condensation in a perovskite lattice at room temperature. *Nat. Phys.* **16**, 301–306 (2020).
- Jayaprakash, R. et al. Two-dimensional organic–exciton polariton lattice fabricated using laser patterning. *ACS Photonics* **7**, 2273–2281 (2020).
- Kim, N. Y. et al. Dynamical d-wave condensation of exciton–polaritons in a two-dimensional square-lattice potential. *Nat. Phys.* **7**, 681–686 (2011).
- Berloff, N. G. et al. Realizing the classical XY Hamiltonian in polariton simulators. *Nat. Mater.* **16**, 1120–1126 (2017).
- Jacqmin, T. et al. Direct observation of Dirac cones and a flatband in a honeycomb lattice for polaritons. *Phys. Rev. Lett.* **112**, 116402 (2014).
- Milčević, M. et al. Orbital edge states in a photonic honeycomb lattice. *Phys. Rev. Lett.* **118**, 107403 (2017).
- Gulevich, D. R., Yudin, D., Iorsh, I. V. & Shelykh, I. A. Kagome lattice from an exciton–polariton perspective. *Phys. Rev. B* **94**, 115437 (2016).
- Lieb, E. H. Two theorems on the Hubbard model. *Phys. Rev. Lett.* **62**, 1201–1204 (1989).
- Zhao, A. & Shen, S.-Q. Quantum anomalous Hall effect in a flat band ferromagnet. *Phys. Rev. B* **85**, 085209 (2012).
- Julku, A., Peotta, S., Vanhala, T. I., Kim, D.-H. & Törmä, P. Geometric origin of superfluidity in the Lieb-lattice flat band. *Phys. Rev. Lett.* **117**, 045303 (2016).
- Sala, V. G. et al. Spin-orbit coupling for photons and polaritons in microstructures. *Phys. Rev. X* **5**, 011034 (2015).
- Dufferwiel, S. et al. Spin textures of exciton–polaritons in a tunable microcavity with large TE–TM splitting. *Phys. Rev. Lett.* **115**, 246401 (2015).
- Klemmt, S. et al. Polariton condensation in S- and P-flatbands in a two-dimensional Lieb lattice. *Appl. Phys. Lett.* **111**, 231102 (2017).
- Whittaker, C. E. et al. Exciton polaritons in a two-dimensional Lieb lattice with spin-orbit coupling. *Phys. Rev. Lett.* **120**, 097401 (2018).
- El Daif, O. et al. Polariton quantum boxes in semiconductor microcavities. *Appl. Phys. Lett.* **88**, 061105 (2006).
- Wertz, E. et al. Spontaneous formation and optical manipulation of extended polariton condensates. *Nat. Phys.* **6**, 860–864 (2010).
- Urbonas, D., Stöferle, T., Scafrimuto, F., Scherf, U. & Mahrt, R. F. Zero-dimensional organic exciton–polaritons in tunable coupled Gaussian defect microcavities at room temperature. *ACS Photonics* **3**, 1542–1545 (2016).
- Baboux, F. et al. Bosonic condensation and disorder-induced localization in a flat band. *Phys. Rev. Lett.* **116**, 066402 (2016).
- Dusel, M. et al. Room temperature organic exciton–polariton condensate in a lattice. *Nat. Commun.* **11**, 2863 (2020).
- Scafrimuto, F., Urbonas, D., Scherf, U., Mahrt, R. F. & Stöferle, T. Room-temperature exciton–polariton condensation in a tunable zero-dimensional microcavity. *ACS Photonics* **5**, 85–89 (2018).
- Sun, M., Savenko, I. G., Flach, S. & Rubo, Y. G. Excitation of localized condensates in the flat band of the exciton–polariton Lieb lattice. *Phys. Rev. B* **98**, 161204 (2018).
- Goblot, V. et al. Nonlinear polariton fluids in a flatband reveal discrete gap solitons. *Phys. Rev. Lett.* **123**, 113901 (2019).
- Yagafarov, T. et al. Mechanisms of blueshifts in organic polariton condensates. *Commun. Phys.* **3**, 1–10 (2020).
- Coles, D. M. et al. Vibrationally assisted polariton–relaxation processes in strongly coupled organic–semiconductor microcavities. *Adv. Funct. Mater.* **21**, 3691–3696 (2011).
- Mazza, L., Kéna-Cohen, S., Michetti, P. & La Rocca, G. C. Microscopic theory of polariton lasing via vibronically assisted scattering. *Phys. Rev. B* **88**, 075321 (2013).
- Zasedatelev, A. V. et al. A room-temperature organic polariton transistor. *Nat. Photon.* **13**, 378–383 (2019).
- Kartashov, Y. V. & Skryabin, D. V. Two-dimensional topological polariton laser. *Phys. Rev. Lett.* **122**, 083902 (2019).

### Acknowledgements

This work was partly supported by the QuantERA project RouTe (SNSF Grant No. 20QT21\_175389) and the H2020 MSCA project Synchronics (SBFI Grant No. 15.0275).

### Author contributions

F.S. performed the optical experiments. D.U. fabricated the sample. F.S., D.U., M.A.B. and T.S. analyzed the data and performed the simulations and modelling. U.S. provided the polymer material. R.F.M. and T.S. supervised the project. All authors contributed to the manuscript and have given approval to the final version of the manuscript.

### Competing interests

The authors declare no competing interests.

### Additional information

**Supplementary information** The online version contains supplementary material available at <https://doi.org/10.1038/s42005-021-00548-w>.

**Correspondence** and requests for materials should be addressed to T.Söf.

**Reprints and permission information** is available at <http://www.nature.com/reprints>

**Publisher's note** Springer Nature remains neutral with regard to jurisdictional claims in published maps and institutional affiliations.



**Open Access** This article is licensed under a Creative Commons Attribution 4.0 International License, which permits use, sharing, adaptation, distribution and reproduction in any medium or format, as long as you give appropriate credit to the original author(s) and the source, provide a link to the Creative Commons license, and indicate if changes were made. The images or other third party material in this article are included in the article's Creative Commons license, unless indicated otherwise in a credit line to the material. If material is not included in the article's Creative Commons license and your intended use is not permitted by statutory regulation or exceeds the permitted use, you will need to obtain permission directly from the copyright holder. To view a copy of this license, visit <http://creativecommons.org/licenses/by/4.0/>.

© The Author(s) 2021